

# Excitonic topology and quantum geometry in organic semiconductors

Wojciech J. Jankowski,<sup>1,\*</sup> Joshua J.P. Thompson,<sup>2,†</sup> Bartomeu Monserrat,<sup>1,2,‡</sup> and Robert-Jan Slager<sup>1,§</sup>

<sup>1</sup>*TCM Group, Cavendish Laboratory, Department of Physics,  
J J Thomson Avenue, Cambridge CB3 0HE, United Kingdom*

<sup>2</sup>*Department of Materials Science and Metallurgy, University of Cambridge,  
27 Charles Babbage Road, Cambridge CB3 0FS, United Kingdom*

(Dated: June 19, 2024)

Excitons drive the optoelectronic properties of organic semiconductors which underpin devices including solar cells and light-emitting diodes. We demonstrate that excitons can exhibit topologically non-trivial states and identify a family of organic semiconductors exhibiting the predicted excitonic topological phases. We also show that the topological phase can be controlled through chemical functionalisation and through the dielectric environment of the material. Appealing to quantum Riemannian geometry, we predict that topologically non-trivial excitons have a lower bound on their centre-of-mass spatial spread, which can significantly exceed the size of a unit cell. The discovery of excitonic topology and excitonic Riemannian geometry in organic materials brings together two mature fields and suggests many new possibilities for a range of future optoelectronic applications.

*Introduction.*— Topology is a versatile tool that drives the study of diverse condensed matter phenomena. Topological invariants arise due to phases acquired by wave functions when adiabatically transported around the Brillouin zone, and provide a classification of states of matter that has radically transformed our understanding of inorganic materials over the past few decades [1, 2]. This work has culminated in a rather complete understanding of free fermionic band structures, which can be characterised through the gluing together of eigenvalues, or irreducible representations, between high symmetry points in the momentum space Brillouin zone [3–6]. Assessing whether this admits an exponentially localised Wannier representation in real space leads to their topological characterisation [7, 8]. Current efforts are moving from free fermion systems towards the question of how these ideas can drive new understanding in interacting systems. An example of an interacting system is that of electron-hole bound states, or excitons.

Excitons dominate the optoelectronic properties of a wide range of materials, particularly those made of weakly interacting organic molecules. Organic semiconductors possess excellent light-harvesting properties, driven by the formation of excitons [9–12], while being chemically versatile [11, 13], cheap, and environmentally friendly to fabricate [14, 15]. These features make organic semiconductors one of the most promising material platforms in which to realise optoelectronic devices, from photovoltaics [16, 17] and light-emitting diodes [18, 19] to biosensors [20]. The electron-hole distance and the centre-of-mass location of excitons can differ greatly between materials, and delocalised excitons with high mobilities are particularly promising for applications [21].

In this work, we establish a link between the rich

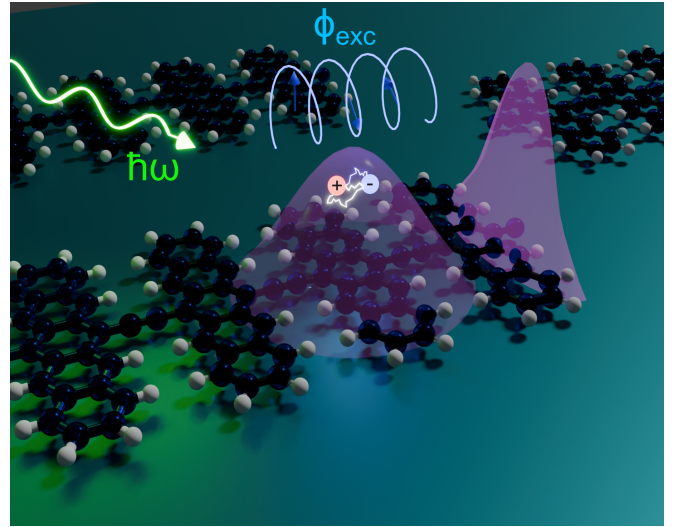


**FIG. 1.** Formation of topological excitons from electron and hole pairs in organic materials, induced by photoexcitation with light. Topological excitons exhibit a winding of the excitonic Bloch vectors  $|u_q^{\text{exc}}\rangle$  as the momentum of the excitons is changed, which is captured by the excitonic Berry phases  $\phi_{\text{exc}}$  and associated inversion symmetry-protected topological  $\mathbb{Z}_2$  invariant  $P_{\text{exc}}$ .

exciton phenomenology in organic semiconductors with novel topological insights of such phases, developing a promising platform in which these ideas could culminate in experimentally viable topological phases and phenomena. In particular, we fully characterise the inversion-symmetry-protected excitonic topology in one-dimensional systems in terms of the excitonic Berry phase and a  $\mathbb{Z}_2$  excitonic topological invariant. Additionally, we derive a lower bound on the spread of the exciton centre-of-mass wavefunction arising from a non-trivial excitonic quantum metric induced by the excitonic topology.

We derive these results using model Hamiltonians and, importantly, we also predict their manifestation in the

\* wjj25@cam.ac.uk;

† jjt56@cam.ac.uk

‡ bm418@cam.ac.uk

§ rjs269@cam.ac.uk

polyacene family of one-dimensional organic semiconductors. We identify material realisations of all predicted topological phases, which can be manipulated both chemically through the lateral size of the polyacene chains and externally through changes in the dielectric environment. Our findings of exotic excitonic states in organic materials bring together organic chemistry, semiconductor physics, and topological condensed matter.

*Excitonic topology and Berry phases.*— The topological character of excitons is fully encoded in the excitonic wavefunction  $|\psi_{\mathbf{q}}^{\text{exc}}\rangle$ . In a periodic crystal, the excitonic wavefunction [22–25] can be decomposed in terms of (i) electronic single-particle Bloch states  $|\psi_{\mathbf{k}}^e\rangle = e^{i\mathbf{k}\cdot\mathbf{r}_e} |u_{\mathbf{k}}^e\rangle$ , (ii) hole single-particle Bloch states  $|\psi_{\mathbf{k}}^h\rangle = e^{i\mathbf{k}\cdot\mathbf{r}_h} |u_{\mathbf{k}}^h\rangle$ , and (iii) an interaction-dependent envelope function  $\psi_{\mathbf{q}}(\mathbf{k})$ ; leading to a coherent superposition of electron-hole pairs:

$$|\psi_{\mathbf{q}}^{\text{exc}}\rangle = \sum_{\mathbf{k}} \psi_{\mathbf{q}}(\mathbf{k}) e^{i\mathbf{k}\cdot(\mathbf{r}_e - \mathbf{r}_h)} |u_{\mathbf{k}+\mathbf{q}/2}^e\rangle |u_{-\mathbf{k}+\mathbf{q}/2}^h\rangle. \quad (1)$$

We also introduce  $|u_{\mathbf{q}}^{\text{exc}}\rangle$  as the cell-periodic part of the excitonic Bloch state  $|\psi_{\mathbf{q}}^{\text{exc}}\rangle = e^{i\mathbf{q}\cdot\mathbf{R}} |u_{\mathbf{q}}^{\text{exc}}\rangle$ , where  $\mathbf{R} = (\mathbf{r}_e + \mathbf{r}_h)/2$  is the centre-of-mass position of the exciton. Notably, the relative position  $\mathbf{r} = \mathbf{r}_e - \mathbf{r}_h$  of the electron and hole enters the excitonic state via phase factors weighted by the envelope amplitudes  $\psi_{\mathbf{k}}(\mathbf{q})$ . The solutions of the single-particle electronic problem for electrons and holes, and of the Wannier equation for the envelope part, fully determine the excitonic wavefunction. The excitonic topology can then be studied from the cell-periodic part  $|u_{\mathbf{q}}^{\text{exc}}\rangle$ , on eliminating the phase factor with the centre-of-mass momentum  $\mathbf{q}$  coupling to the centre-of-mass position  $\mathbf{R}$ .

Consistently with K-theory [5, 26], which provides classifications that are stable up to adding an arbitrary number of trivial bands to the system, in the presence of inversion symmetry we can obtain an excitonic  $\mathbb{Z}_2$  invariant  $P_{\text{exc}} = \phi_{\text{exc}}/\pi \bmod 2$  from a Berry phase defined in one spatial dimension [27]:

$$\phi_{\text{exc}} = \int_{\text{BZ}} dq A_{\text{exc}}(q), \quad (2)$$

where  $A_{\text{exc}}(q) = i \langle u_q^{\text{exc}} | \partial_q u_q^{\text{exc}} \rangle$  is the excitonic Berry connection. Alternatively, the excitonic  $\mathbb{Z}_2$  invariant can be re-written as [28]:

$$P_{\text{exc}} = \frac{1}{\pi} \int_{\text{hBZ}} dq [A_{\text{exc}}(q) + A_{\text{exc}}(-q)], \quad (3)$$

with the integration performed over a half Brillouin zone (hBZ) because the inversion symmetry relates the excitonic bands at  $q$  and  $-q$ . The  $\mathbb{Z}_2$  nature of the invariant can be understood intuitively: at the inversion-symmetry-invariant momenta,  $q = 0$  and  $q = \pi$ , the excitonic eigenvectors  $|u_q^{\text{exc}}\rangle$  have the same relative phase in the trivial excitonic regime, whereas in the topological regime these have opposite inversion eigenvalues related

by a  $\pi$  phase. The invariant  $P_{\text{exc}}$  precisely distinguishes two different topologies which are not transversable from one to another without closing a gap in the excitonic bands, similarly to the inversion-protected topology of electrons necessitating a gap closure for a topological phase transition to occur.

*Phase diagram.*— To explore exciton topology in a one-dimensional setting, we consider the excitonic Wannier equation for the envelope function  $\psi_q(k)$ :

$$\sum_{k'} h_{k,k'}(q) \psi_q(k) = E(q) \psi_q(k), \quad (4)$$

where  $E(q)$  is the exciton binding energy and  $h_{k,k'}(q) = (E_{k+q/2}^e - E_{k-q/2}^h) \delta_{k,k'} - W_{k,-k',q}$  includes the single-particle energies for the electrons  $E_{k+q/2}^e$  and holes  $E_{k-q/2}^h$  and the electron-hole interaction  $W_{k,-k',q}$ . For the single-particle electron and hole states we use the Su-Schrieffer-Heeger (SSH) model [29, 30]:

$$H = -t_1 \sum_j c_{B,j}^\dagger c_{A,j} - t_2 \sum_j c_{B+1,j}^\dagger c_{A,j} + \text{h.c.}, \quad (5)$$

with  $c_{B,j}^\dagger/c_{A,j}$  the creation/annihilation operators for the electrons at sublattices  $A, B$ , in unit cell  $j$ , and staggered hopping parameters  $t_1$  and  $t_2$ , where we define the origin of a unit cell such that  $t_1$  is the intracell hopping and  $t_2$  is a hopping across the boundary of the unit cell. Importantly, we also identify a family of organic acene one-dimensional polymers as candidate materials [31, 32], to realise the predicted exciton topological phases, for which we describe the single-particle states using density functional theory [33, 34].

By numerically solving the Wannier equation, we construct the excitonic phase diagram as a function of single-particle states characterised by the hopping parameters  $t_1$  and  $t_2$ , as shown in Fig. 2(a). The phase diagram exhibits three different regimes that are determined by the interplay between single-particle electronic and hole, and excitonic topological invariants. Additionally, we fit the Wannierised low-energy bands of multiple polyacenes to the tight-binding SSH model to identify their location on the phase diagram.

In region I, corresponding to  $t_1 > t_2$ , we have trivial electrons and holes yielding trivial excitons. This is a consequence of the absence of winding in the vectors  $|u_{\mathbf{k}}^e\rangle$  and  $|u_{\mathbf{k}}^h\rangle$  that leads to a trivial electronic Berry phase with  $\phi_e = 0$  and to electronic Wannier centres localised at the centres of the unit cells [35]. In region II, corresponding to  $t_1 < t_2$ , we have topological electrons and holes, resulting in topological excitons, whose topological character is inherited from the underlying electron and hole topology. Explicitly, we have  $\phi_{\text{exc}} = \phi_e = \phi_h = \pi$ , where  $\phi_e$  and  $\phi_h$  are single-particle Berry phases of electrons and holes, respectively. In region III, also corresponding to  $t_1 < t_2$ , we obtain  $\phi_{\text{exc}} = 0$ , despite the presence of non-trivial electrons and holes with  $\phi_e = \phi_h = \pi$ .

In this regime, the electron-hole interaction is the dominant energy scale and it trivialises the excitonic topology, as explained below. Additionally, the excitons are shifted with respect to the electrons and holes constituting them [36]. Intuitively, electrons and holes from different unit cells combine to give excitons with the centre of mass in-between them, as manifested by the corresponding electron, hole, and excitonic Wannier centres given by the Zak phases (see Fig. 3).

In the phase diagram of Fig. 2(a), we indicate where polyanthracene ( $N = 3$ ) and polypentacene ( $N = 5$ ) lie, providing material realisation of both trivial and topological excitonic phases. Polyheptacene ( $N = 7$ ) also falls within region II, but it exhibits relatively flat bands with  $t_1 < 0.2$  eV and therefore falls outside the range plotted in Fig. 2(a). Interestingly, the excitonic topology of the acenes can be controlled through the dielectric screening strength as illustrated for polypentacene in Fig. 2(b) and for polyheptacene in Fig. 2(c). Therefore, it should be possible to experimentally control exciton topological order by changing the dielectric environment of materials. For example, free standing polypentacene sits in the excitonic topological region II of the phase diagram, but increasing dielectric screening through a  $\text{SiO}_2$  substrate or hBN encapsulation drives it towards the excitonic trivial phase in region III, as illustrated in Figure 2(b). In an experimental setting, the screening strength can be controlled through substrate choice, but also through chemical functionalisation and solution, providing readily available tools to explore the phase diagram in Fig. 2(a).

*Characterisation of topological excitons.*— To gain a deeper understanding of the exciton topology and phase diagram presented in Fig. 2, we phenomenologically capture the electron-hole interaction through a dualisation picture using a SSH-Hubbard-like model with a hierarchy of electronic density-density interactions  $U_i$ , with  $i = 1, 2, 3, \dots$  labelling interactions between  $n^{\text{th}}$  order left neighbours for odd  $i$ , and right  $n^{\text{th}}$  order neighbours for even  $i$ . We show that in the limits of vanishing interactions, as well as very high interaction strengths compared with the hopping energies, the physics is effectively captured by the above interacting SSH model either in terms of electronic degrees of freedom or in terms of “dual” density degrees of freedom.

To concretise this phenomenological picture for the bottom exciton band, two limits are of central importance. In the first limit, we consider an interaction smaller than the bandwidth  $U_i \ll t_1, t_2$ , obtaining the standard SSH model [29, 30]. For  $t_2 < t_1$ , we obtain vanishing Berry phases for electrons, holes, and excitons, with all of them localised at the origin of the unit cell [Fig. 3(a)], and corresponding to region I of Fig. 2. For  $t_2 > t_1$ , and in this dispersive limit, the electrons, holes, and as a consequence, the excitons, all acquire  $\pi$  Berry phases, which is also reflected by the inversion-symmetry protected shift of all with respect to the unit cell origin [Fig. 3(b)], corresponding to region II of Fig. 2.

The other limit corresponds to dominant interactions.

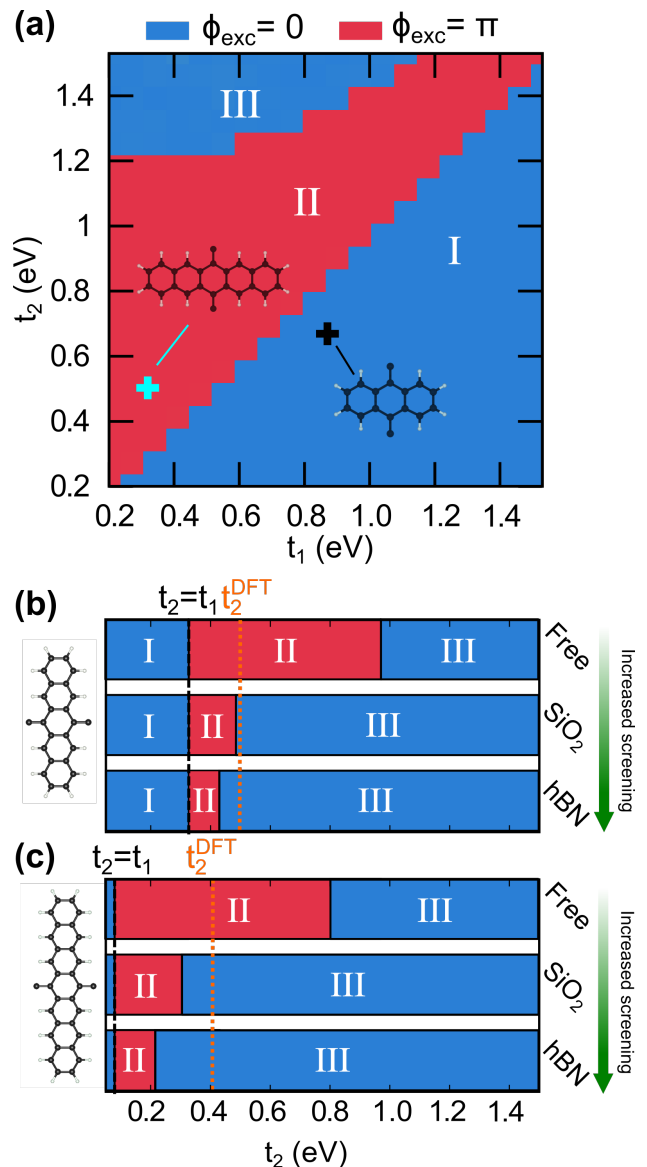


**FIG. 2.** (a) Phase diagram showing excitonic topological phases as a function of  $t_1$  and  $t_2$ , with  $L = 0.8$  nm and  $\alpha_{1\text{D}} = 0.05$  eVÅ. The phase regimes are defined as I, II, and III as discussed in the main text. We also indicate the location of polyanthracene (black cross) and polypentacene (cyan cross) in the phase diagram. (b,c) Phase diagram cuts for fixed  $t_1$  for (b) polypentacene and (c) polyheptacene, on different background dielectrics. For these diagrams, we use material specific parameters  $t_1$  and  $L$  extracted from DFT, and  $t_2$  is marked on the phase diagram with the orange dotted line.

This regime is characterised by flat bands ( $t_2 \gg t_1$  or  $t_2 \ll t_1$ ) and the interactions take the dominant role  $U_i \gg t_1, t_2$ , for  $i = 1, 2$ . The electronic hopping terms become negligible and the nearest-neighbour interactions, modelled with the Hubbard terms, take over the role of the quasiparticle hoppings, with density operators taking the role of creation and annihilation operators after a particle-hole transformation ( $h_{A/B}^\dagger = c_{A/B}$ ) and a boson-

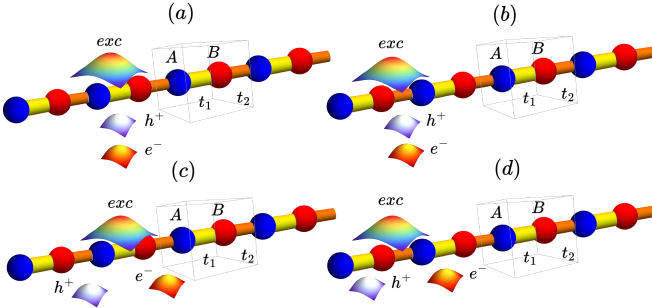


**FIG. 3.** Real space realisation of different combinations of Wannier centre shifts corresponding to the Berry phases of electrons, holes, and excitons, with the interaction-driven mechanisms of the formation of topological and trivial excitons elucidated schematically. **(a)** Trivial electrons and holes forming trivial excitons ( $P_{\text{exc}} = 0$ ) in few-ring polyacenes. **(b)** Topological electrons and holes forming topological excitons ( $P_{\text{exc}} = 1$ ) in many-ring polyacenes. **(c)** Topological electrons and holes forming trivial excitons ( $P_{\text{exc}} = 0$ ) in largest-ring polyacenes with nearly-flat bands. In this case the excitons exhibit a trivialised excitonic Berry phase due to the interaction of obstructed electrons and holes shifted from the origin. **(d)** Topological excitons ( $P_{\text{exc}} = 1$ ) formed out of trivial electrons and holes. Cases **(a)**-**(c)** are realised in the lowest excitonic band of polyacenes, while **(d)** only appears for the higher excitonic bands.

isation to the localised exciton basis ( $b_{A/B}^\dagger = c_{A/B}^\dagger h_{A/B}^\dagger$ ), as detailed in the Appendix. On relabelling the dominant nearest-neighbour interaction energies  $U_1$  and  $U_2$  as  $2t_1^{\text{exc}}$  and  $2t_2^{\text{exc}}$ , the dual Hamiltonian takes an SSH form:

$$H = -t_1^{\text{exc}} \sum_j b_{B,j}^\dagger b_{A,j} - t_2^{\text{exc}} \sum_j b_{B+1,j}^\dagger b_{A,j} + \text{h.c.} \quad (6)$$

Diagonalizing this effective dual Hamiltonian with excitonic states directly gives the excitonic eigenvectors  $|\psi_q^{\text{exc}}\rangle$  without reference to the envelope function which results from the Wannier equation, and allowing us to directly compute the excitonic  $\mathbb{Z}_2$  invariant  $P_{\text{exc}}$  and the excitonic Berry phase  $\phi_{\text{exc}}$ .

With the dual Hamiltonian in Eq. (6), we obtain the topology of region III when  $t_2 \gg t_1$  and  $t_1^{\text{exc}} > t_2^{\text{exc}}$ , as well as the part of region I with ( $t_1 \ll t_2$ ). We stress that the rest of region I (where the bandwidth is larger than  $U_i$ ) and region II are a consequence of the electronic SSH Hamiltonian in the opposite limit, where the excitons directly inherit the topology of electrons and holes, without any additional interaction-driven effects, which are negligible in these parts of the phase diagram.

The above arguments allow us to reconstruct the above limiting cases and thus the different sectors I, II, and III of the phase diagram relevant for a realistic  $\mathbb{Z}_2$  excitonic topological organic semiconductor. We note that we do not retrieve a region with trivial electronic and hole Berry phases ( $\phi_e = \phi_h = 0$ ) and topological excitons  $\phi_{\text{exc}} = \pi$  in the lowest excitonic band. Interestingly, this regime can in principle be obtained in a similar model in the limit

$U_2 > U_1 \gg t_2$ , and with  $t_1 \gg t_2$ , as demonstrated recently in Ref. [36]. However, in real materials, the single-particle parameters  $t_1$  and  $t_2$  and the exciton parameters  $t_1^{\text{exc}}$  and  $t_2^{\text{exc}}$  might not be independent, and we do not find this regime in our phase diagram in Fig. 2.

Additionally, we can utilise our model analysis to capture the phenomenology of the shifting of the boundary between region II and region III in the strong screening limit. The intuitive picture is that in the presence of a strongly polar substrate, the interaction between the electrons and holes within the organic material becomes screened, and the weakly interacting electrons and holes in different cells form excitons with the centre of mass residing centrally in-between, see Fig. 3(c). Effectively, the described pinning of the excitons is imposed by an external substrate, which we also quantitatively detail in the Appendix. As such, there is a mismatch between the Berry phases, or equivalently Wannier centre positions of the electrons and holes, known to reflect the electric polarisation associated with the charge distribution in the material [37], compared to the excitons. This culminates in the topology of region III, consistently with the numerical results. While the qualitative theoretical argument above does not require the numerical solution of the Wannier equation to deduce the topological structure of the excitonic phase diagram, a full numerical solution is however necessary to quantitatively build the topological excitonic phase diagram boundaries between regions II and III, as shown in Fig. 2.

*Excitonic quantum geometry.*— The excitonic topology described above has a direct implication on a geometric property, the spread (variance) of the excitonic states in the centre-of-mass coordinate  $\mathbf{R}$ . To understand this relation, we consider the quantum metric  $g_{ij}$  [38, 39], which is a tensor made of symmetrised derivatives of momentum-space Bloch states, and defined as:

$$g_{ij}^{\text{exc}} = \frac{1}{2} \left[ \langle \partial_{q_i} u_{\mathbf{q}}^{\text{exc}} | 1 - \hat{P} | \partial_{q_j} u_{\mathbf{q}}^{\text{exc}} \rangle + \text{c.c.} \right], \quad (7)$$

where  $\hat{P} = |u_{\mathbf{q}}^{\text{exc}}\rangle \langle u_{\mathbf{q}}^{\text{exc}}|$  is a projector onto the exciton band of interest. More generally, it can be considered to be the real part of a Hermitian quantum geometric tensor (QGT) [38, 40], which can be written as [38, 41]:

$$Q_{ij}^{\text{exc}} = \langle \partial_{q_i} u_{\mathbf{q}}^{\text{exc}} | 1 - \hat{P} | \partial_{q_j} u_{\mathbf{q}}^{\text{exc}} \rangle, \quad (8)$$

The imaginary part of the QGT corresponds to the Berry curvature, encoding the topology, which underlies quantum Hall phenomena, while the positive-semidefiniteness of the QGT equips the metric and the Berry curvature with a set of physical bounds related to optics, superconductivity, and quantum transport [40]. The geometric meaning of the metric can be further identified by defining a Fubini-Study metric [38]  $ds^2 = 1 - \left| \langle u_{\mathbf{q}}^{\text{exc}} | u_{\mathbf{q}+\mathbf{d}\mathbf{q}}^{\text{exc}} \rangle \right|^2$  and recognizing that

$$ds^2 = g_{ij}^{\text{exc}} dq^i dq^j, \quad (9)$$

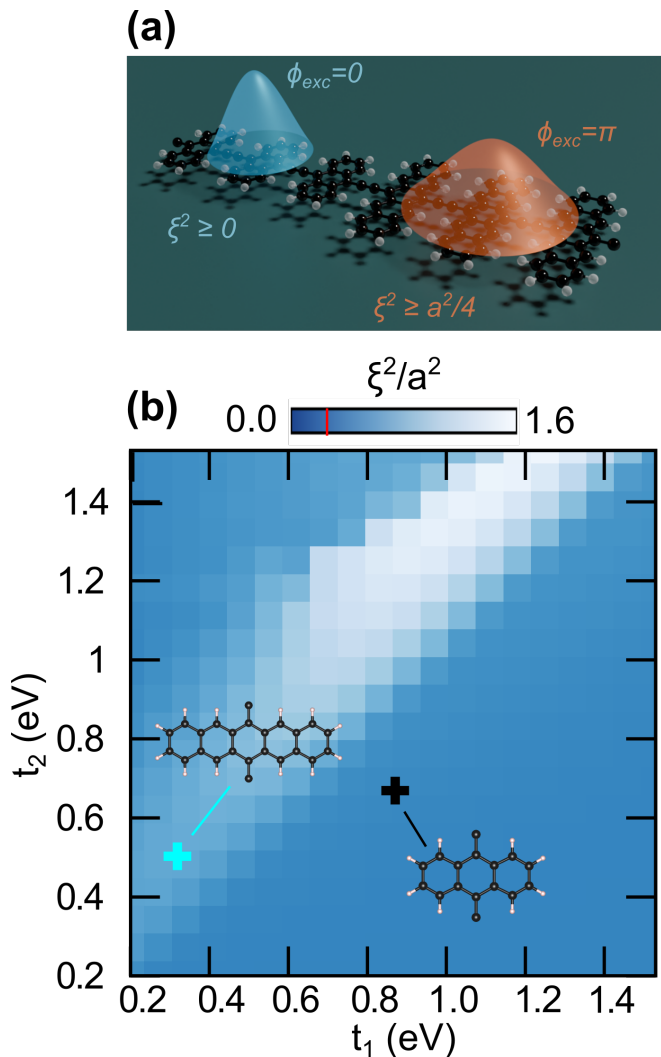


**FIG. 4.** (a) Illustration of topological (orange) and trivial (blue) excitons in polyacenes with the corresponding excitonic Berry phases and excitonic Wannier state spreads bounded below by the excitonic quantum metric. (b) Spread of the excitonic Wannier states  $\xi^2$  as a function of the single-particle hopping parameters  $t_1$  and  $t_2$ , with the excitonic phase bounded by the excitonic quantum geometry (red line in gradient bar).

which is reminiscent of the well-known relation between the metric and the spacetime intervals in general relativity, and where the Einstein summation convention is implicitly assumed.

In the context of excitons, the metric maps to the variance of the maximally-localised excitonic Wannier functions (MLXWF) [42] in real space. In this regard, we numerically demonstrate the spread of the excitons in Fig. 4. We observe that whenever the topological excitonic invariant  $P_{exc}$  is non-trivial, the diameter associated with the variance of the real space exciton wavefunctions necessarily needs to exceed the size of the unit cell due to the non-trivial topology set by the quantized Berry phase. Specifically, as illustrated in Fig. 3, we find

that for an excitonic inversion invariant  $P_{exc} = 0$ , the excitons are localised inside the unit cell at its centre and have no lower bound on their spread.

The connection between the exciton spread and the metric can be quantified by a bound set by an integral of the quantum metric,  $\oint dq g_{xx}^{exc}$ , where in one dimension, which we refer to as the  $x$ -direction, only the  $g_{xx}$  component exists. Using a Cauchy-Schwartz type inequality, we find:

$$\xi^2 \geq \frac{a^2 P_{exc}^2}{4}, \quad (10)$$

where  $a$  is the unit cell length and  $\xi^2 \equiv \text{Var } R = \langle R^2 \rangle - \langle R \rangle^2$  is the variance with respect to the MLXWF center. This relation explicitly shows that the size of topological excitons, as captured by the spread of the excitonic Wannier functions, should be comparable to, or even exceeding, the size of the unit cell, matching the numerical results. That is, topological excitons with  $P_{exc} = 1$  are shifted to the boundary of the unit cell  $\langle R \rangle = a/2$  and their spread  $\xi^2 \equiv \text{Var } R = \langle R^2 \rangle - \langle R \rangle^2$  is bound from below, resulting in the centre-of-mass  $R$  of an exciton being localised within a characteristic length  $\xi \sim a/2$ . In the presence of a localised electron or hole (e.g. through defect pinning), the bound on the delocalisation of the centre-of-mass  $R$  position also determines the effective size of the exciton characterised by the electron-hole distance  $r$ . This is consistent with the observed transition from localised “Frenkel” to spread out “Mott-Wannier” excitons in polyacenes [32]. Finally, we note that the quantum-geometric bound due to excitonic band topology persists in the higher excitonic bands, see Fig. 5. In the higher bands, quantum geometry takes a more dominant role, even without the presence of non-trivial topology, due to the contributions of alternating envelope functions of the weaker-bound higher energy excitonic states, as we describe in Appendix.

*Discussion.*— Our findings open up multiple research avenues. From a theoretical point of view, the SSH-like topology discussed above, also referred to as obstructed insulators, is the simplest kind of topology. Extending the study of topological excitons to higher dimensional systems and to materials with different types of (crystalline) symmetries is expected to greatly expand excitonic topology and quantum geometry [23–25, 36, 41]. Another interesting research direction is to extend the discussion above to spinful systems, which would enable a distinction between singlet and triplet excitons.

Moreover, higher excitonic bands (see Fig. 5) in the studied polyacene systems also exhibit the excitonic topology and non-trivial quantum geometry. Here, the flipping of regions with  $P_{exc} = 0$  and  $P_{exc} = 1$  can be explained with the change of the shape of the excitonic envelope functions, as deduced from solving the Wannier equation. Namely, at the level of the Wannier equation, the envelope determines  $U_i$ , which in turn contribute to  $\phi_{exc}$ , as detailed in Appendix. For higher excitonic bands, the dualised theoretical picture still holds

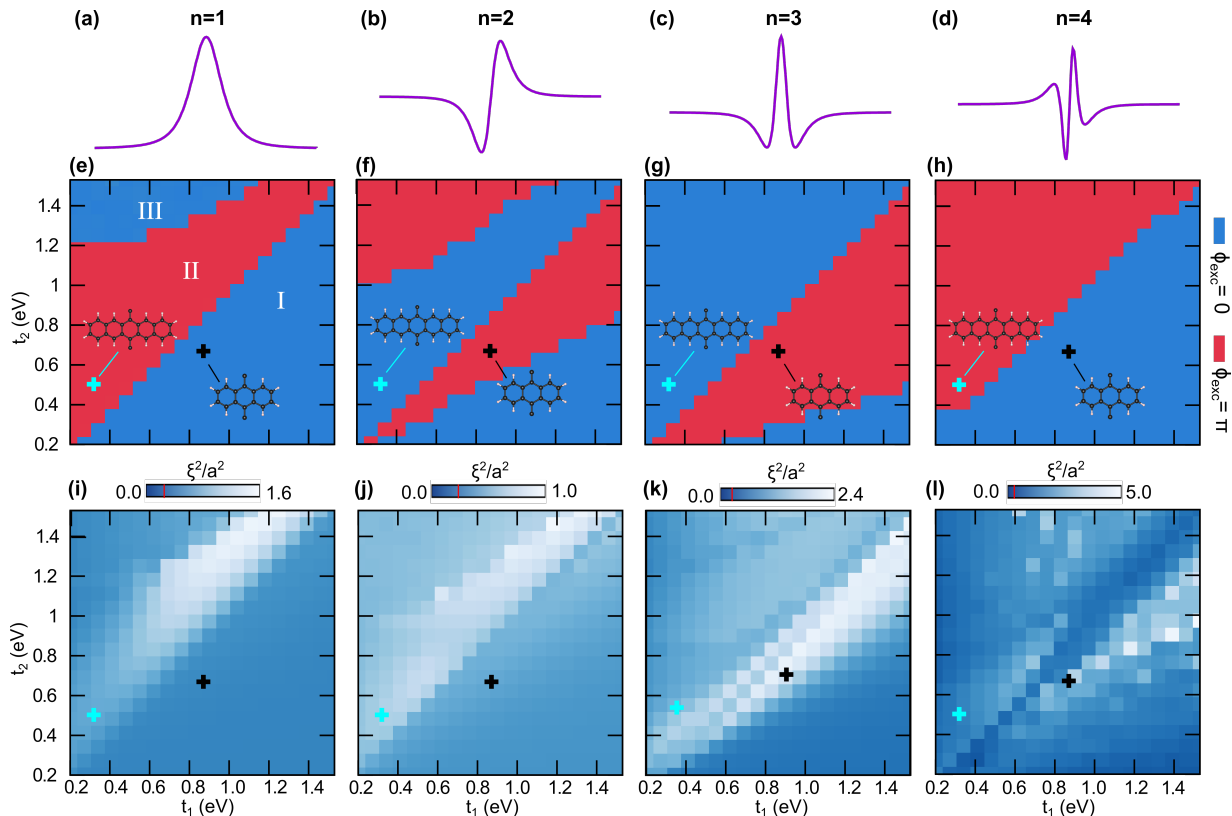


**FIG. 5.** (a-d) Envelope functions  $\psi_{q=0}(k)$  for different excitonic bands  $n = 1, 2, 3, 4$ , respectively. (e-h) Topological excitonic phase diagram as a function of the hopping parameters  $t_1$  and  $t_2$ , highlighting regions with different invariant  $P_{\text{exc}} = \phi_{\text{exc}}/\pi \bmod 2$  and identifying the location of various polyacenes. The excitons in polypentacene (cyan cross) and polyheptacene (black cross) realise different excitonic topologies. (i-l) Spread of the excitonic Wannier states  $\xi^2$ , with the excitonic topological phases bounded by the excitonic quantum geometry (red line in gradient bar). Although the numerical results match the general theory and topological phase diagram intimately, we note that in higher excitonic bands  $n = 3, 4$  (k-l) there is a larger spread in the excitonic wavefunctions due to the non-trivial quantum geometry induced by the more delocalised envelope function, even when the topology of the exciton is trivial (see main text).

by the same argument as for the lowest excitonic bands, although the  $U_i$  terms compare differently, which can change the excitonic topology and phase diagram. In particular, we note that unlike in the lowest excitonic band, a fourth region with trivial electrons and holes, but with topological excitons [36], emerges for the first higher excitonic bands ( $n = 2, 3$ ), which is manifested in polyanthracene ( $N = 3$ ). Again, the dielectric screening can shift the excitonic phase diagram boundaries, showing that a modification of the substrate can also change the topology of higher excitonic bands in organic materials.

These potential theoretical extensions would naturally fit with active areas of experimental exciton research. Excitons are experimentally studied through their optical, dynamics, and transport properties, using techniques such as pump-probe experiments. The findings reported above already anticipate some potential experimental manifestations of exciton topology. First, the distinct excitonic topology exhibited by the different excitonic states (see Fig. 5) suggests that optical probes

could selectively target different excitonic behaviour in the same material, as well as unusual dynamics as the excitons relax towards the lowest energy state following photoexcitation. Second, the lower bound set on the exciton size by quantum geometry (see Fig. 4) suggests that transport will be enhanced for topological excitons compared to their trivial counterparts. Third, a hallmark of topology is the so-called bulk-boundary correspondence, in which the bulk topology is associated with unusual boundary states that are often protected against scattering and support dissipationless transport. In the case of excitons, these boundary states should be manifested in terms of dipole currents.

From the materials point of view, the interplay between topology, excitons, and organic polyacenes reported above is only the starting point. Organic semiconductors provide a more general platform to explore exciton topology, with organic semiconductors in one, two, and three dimensions often exhibiting strongly bound excitons. Additionally, it should be possible to harness the decades of experience in organic chemistry to manipu-

late organic semiconductors to explore many potential different excitonic topological regimes, such as those described above (Fig. 2), but notably also richer topologies in higher dimensions. Beyond organic semiconductors, inorganic two-dimensional materials and van der Waals bonded layered materials also exhibit strongly bound excitons, providing additional materials platforms to explore excitonic topology.

*Conclusions.*— Overall, we establish a connection between topological ideas, common in the study of electronic phases, and the field of excitons in organic semiconductors. We describe a simple proof-of-principle for exciton topology in the form of one dimensional winding numbers, constructing a full exciton topology phase diagram with different regimes reflecting the interplay between the underlying (so-called obstructed) electron and hole topologies with the new exciton topology. We also present a family of organic polymers that host the predicted exciton topologies, and demonstrate the manipulation of this topology by controlling the dielectric screening through substrate choice. Finally, we discover that exciton topology is related to the spatial localisation of excitons, as determined by Riemannian metric identities. In particular, we find a lower bound on the exciton

size for topologically non-trivial excitons. Our results set a benchmark for a potentially rich exploration of topological excitons in organic semiconductors and beyond.

## ACKNOWLEDGMENTS

The authors thank Richard Friend, Akshay Rao, Sun-Woo Kim, Gaurav Chaudhary, Arjun Ashoka, and Frank Schindler for helpful discussions. W.J.J. acknowledges funding from the Rod Smallwood Studentship at Trinity College, Cambridge. J.J.P.T. and B.M. acknowledge support from a EPSRC Programme Grant [EP/W017091/1]. B.M. also acknowledges support from a UKRI Future Leaders Fellowship [MR/V023926/1], from the Gianna Angelopoulos Programme for Science, Technology, and Innovation, and from the Winton Programme for the Physics of Sustainability. R.-J.S. acknowledges funding from a New Investigator Award, EPSRC grant EP/W00187X/1, a EPSRC ERC underwrite grant EP/X025829/1, and a Royal Society exchange grant IES/R1/221060 as well as Trinity College, Cambridge.

- 
- [1] Xiao-Liang Qi and Shou-Cheng Zhang, “Topological insulators and superconductors,” *Rev. Mod. Phys.* **83**, 1057–1110 (2011).
- [2] M. Z. Hasan and C. L. Kane, “Colloquium: Topological Insulators,” *Rev. Mod. Phys.* **82**, 3045–3067 (2010).
- [3] Liang Fu, “Topological Crystalline Insulators,” *Phys. Rev. Lett.* **106**, 106802 (2011).
- [4] Robert-Jan Slager, Andrej Mesaros, Vladimir Juričić, and Jan Zaanen, “The space group classification of topological band-insulators,” *Nat. Phys.* **9**, 98 (2012).
- [5] Jorrit Kruthoff, Jan de Boer, Jasper van Wezel, Charles L. Kane, and Robert-Jan Slager, “Topological Classification of Crystalline Insulators through Band Structure Combinatorics,” *Phys. Rev. X* **7**, 041069 (2017).
- [6] Liang Fu, C. L. Kane, and E. J. Mele, “Topological Insulators in Three Dimensions,” *Phys. Rev. Lett.* **98**, 106803 (2007).
- [7] Hoi Chun Po, Ashvin Vishwanath, and Haruki Watanabe, “Symmetry-based indicators of band topology in the 230 space groups,” *Nat. Commun.* **8**, 50 (2017).
- [8] Barry Bradlyn, L. Elcoro, Jennifer Cano, M. G. Vergniory, Zhijun Wang, C. Felser, M. I. Aroyo, and B. Andrei Bernevig, “Topological quantum chemistry,” *Nature* **547**, 298 (2017).
- [9] Michael Kasha, Henry R Rawls, and M Ashraf El-Bayoumi, “The exciton model in molecular spectroscopy,” *Pure and Applied Chemistry VIIIth* **11**, 371–392 (1965).
- [10] Oleksandr V Mikhnenko, Paul WM Blom, and Thuc-Quyen Nguyen, “Exciton diffusion in organic semiconductors,” *Energy & Environmental Science* **8**, 1867–1888 (2015).
- [11] Caterina Cocchi, Tobias Breuer, Gregor Witte, and Claudia Draxl, “Polarized absorbance and Davydov splitting in bulk and thin-film pentacene polymorphs,” *Physical Chemistry Chemical Physics* **20**, 29724–29736 (2018).
- [12] Joshua JP Thompson, Dominik Muth, Sebastian Anhäuser, Daniel Bischof, Marina Gerhard, Gregor Witte, and Ermin Malic, “Singlet-exciton optics and phonon-mediated dynamics in oligoacene semiconductor crystals,” *Natural Sciences* **3**, e20220040 (2023).
- [13] Daniel William Davies, Sang Kyu Park, Prapti Kafle, Hyunjoong Chung, Dafei Yuan, Joseph W Strzalka, Stefan CB Mannsfeld, SuYin Grass Wang, Yu-Sheng Chen, Danielle L Gray, *et al.*, “Radically tunable n-type organic semiconductor via polymorph control,” *Chemistry of Materials* **33**, 2466–2477 (2021).
- [14] Sybille Allard, Michael Forster, Benjamin Souharce, Heiko Thiem, and Ullrich Scherf, “Organic semiconductors for solution-processable field-effect transistors (ofets),” *Angewandte Chemie International Edition* **47**, 4070–4098 (2008).
- [15] Seth B Darling and Fengqi You, “The case for organic photovoltaics,” *Rsc Advances* **3**, 17633–17648 (2013).
- [16] Daniel N Congreve, Jiye Lee, Nicholas J Thompson, Eric Hontz, Shane R Yost, Philip D Reuswig, Matthias E Bahlke, Sebastian Reineke, Troy Van Voorhis, and Marc A Baldo, “External quantum efficiency above 100% in a singlet-exciton-fission-based organic photovoltaic cell,” *Science* **340**, 334–337 (2013).
- [17] Lulu Sun, Kenjiro Fukuda, and Takao Someya, “Recent progress in solution-processed flexible organic photovoltaics,” *npj Flexible Electronics* **6**, 89 (2022).
- [18] Ji-Seon Kim, Peter KH Ho, Neil C Greenham, and Richard H Friend, “Electroluminescence emission pattern

- of organic light-emitting diodes: Implications for device efficiency calculations,” *Journal of Applied Physics* **88**, 1073–1081 (2000).
- [19] Hwan-Hee Cho, Daniel G Congrave, Alexander J Gillett, Stephanie Montanaro, Haydn E Francis, Víctor Riesgo-Gonzalez, Junzhi Ye, Rituparno Chowdury, Weixuan Zeng, Marc K Etherington, *et al.*, “Suppression of Dexter transfer by covalent encapsulation for efficient matrix-free narrowband deep blue hyperfluorescent oleds,” *Nature Materials* **23**, 519–526 (2024).
- [20] Polina Jacoutot, Alberto D Scaccabarozzi, Tianyi Zhang, Zhuoran Qiao, Filip Aniés, Marios Neophytou, Helen Bristow, Rhea Kumar, Maximilian Moser, Alkmini D Nega, *et al.*, “Infrared organic photodetectors employing ultralow bandgap polymer and non-fullerene acceptors for biometric monitoring,” *Small* **18**, 2200580 (2022).
- [21] Alexander J Sneyd, David Beljonne, and Akshay Rao, “A new frontier in exciton transport: transient delocalization,” *The Journal of Physical Chemistry Letters* **13**, 6820–6830 (2022).
- [22] Wang Yao and Qian Niu, “Berry phase effect on the exciton transport and on the exciton Bose-Einstein condensate,” *Phys. Rev. Lett.* **101**, 106401 (2008).
- [23] Jinlyu Cao, H. A. Fertig, and Luis Brey, “Quantum geometric exciton drift velocity,” *Phys. Rev. B* **103**, 115422 (2021).
- [24] Yves H. Kwan, Yichen Hu, Steven H. Simon, and S. A. Parameswaran, “Exciton band topology in spontaneous quantum anomalous Hall insulators: Applications to twisted bilayer graphene,” *Phys. Rev. Lett.* **126**, 137601 (2021).
- [25] Lucas Maisel Licerán, Francisco García Flórez, Laurens D. A. Siebbeles, and Henk T. C. Stoof, “Single-particle properties of topological Wannier excitons in bismuth chalcogenide nanosheets,” *Scientific Reports* **13**, 6337 (2023).
- [26] A. Kitaev, “Periodic table for topological insulators and superconductors,” *AIP Conf. Proc.* **1134**, 22 (2009).
- [27] J. Zak, “Berry’s phase for energy bands in solids,” *Phys. Rev. Lett.* **62**, 2747–2750 (1989).
- [28] Taylor L. Hughes, Emil Prodan, and B. Andrei Bernevig, “Inversion-symmetric topological insulators,” *Phys. Rev. B* **83**, 245132 (2011).
- [29] W. P. Su, J. R. Schrieffer, and A. J. Heeger, “Solitons in polyacetylene,” *Phys. Rev. Lett.* **42**, 1698–1701 (1979).
- [30] W. P. Su, J. R. Schrieffer, and A. J. Heeger, “Soliton excitations in polyacetylene,” *Phys. Rev. B* **22**, 2099–2111 (1980).
- [31] Borja Cirera, Ana Sánchez-Grande, Bruno de la Torre, José Santos, Shayan Edalatmanesh, Eider Rodríguez-Sánchez, Koen Lauwaet, Benjamin Mallada, Radek Zbořil, Rodolfo Miranda, *et al.*, “Tailoring topological order and  $\pi$ -conjugation to engineer quasi-metallic polymers,” *Nature nanotechnology* **15**, 437–443 (2020).
- [32] D. Romanin, M. Calandra, and A. W. Chin, “Excitonic switching across a  $F_2$  topological phase transition: From Mott-Wannier to Frenkel excitons in organic materials,” *Phys. Rev. B* **106**, 155122 (2022).
- [33] P. Hohenberg and W. Kohn, “Inhomogeneous electron gas,” *Phys. Rev.* **136**, B864–B871 (1964).
- [34] R. O. Jones, “Density functional theory: Its origins, rise to prominence, and future,” *Rev. Mod. Phys.* **87**, 897–923 (2015).
- [35] Nicola Marzari, Arash A. Mostofi, Jonathan R. Yates, Ivo Souza, and David Vanderbilt, “Maximally localized Wannier functions: Theory and applications,” *Rev. Mod. Phys.* **84**, 1419–1475 (2012).
- [36] Henry Davenport, Johannes Knolle, and Frank Schindler, “Interaction-induced crystalline topology of excitons,” (2024), [arXiv:2405.19394](https://arxiv.org/abs/2405.19394) [[cond-mat.mes-hall](https://arxiv.org/abs/2405.19394)].
- [37] RD King-Smith and David Vanderbilt, “Theory of polarization of crystalline solids,” *Phys. Rev. B* **47**, 1651 (1993).
- [38] JP Provost and G Vallee, “Riemannian structure on manifolds of quantum states,” *Communications in Mathematical Physics* **76**, 289–301 (1980).
- [39] R. Resta, “The insulating state of matter: a geometrical theory,” *The European Physical Journal B* **79**, 121–137 (2011).
- [40] Päivi Törmä, “Essay: Where can quantum geometry lead us?” *Phys. Rev. Lett.* **131**, 240001 (2023).
- [41] Adrien Bouhon, Abigail Timmel, and Robert-Jan Slager, “Quantum geometry beyond projective single bands,” (2023), [arXiv:2303.02180](https://arxiv.org/abs/2303.02180) [[cond-mat.mes-hall](https://arxiv.org/abs/2303.02180)].
- [42] Jonah B. Haber, Diana Y. Qiu, Felipe H. da Jornada, and Jeffrey B. Neaton, “Maximally localized exciton Wannier functions for solids,” *Phys. Rev. B* **108**, 125118 (2023).
- [43] Paolo Giannozzi, Stefano Baroni, Nicola Bonini, Matteo Calandra, Roberto Car, Carlo Cavazzoni, Davide Ceresoli, Guido L Chiarotti, Matteo Cococcioni, Ismaila Dabo, Andrea Dal Corso, Stefano de Gironcoli, Stefano Fabris, Guido Fratesi, Ralph Gebauer, Uwe Gerstmann, Christos Gougoussis, Anton Kokalj, Michele Lazzeri, Layla Martin-Samos, Nicola Marzari, Francesco Mauri, Riccardo Mazzarello, Stefano Paolini, Alfredo Pasquarello, Lorenzo Paulatto, Carlo Sbraccia, Sandro Scandolo, Gabriele Sclauzero, Ari P Seitsonen, Alexander Smogunov, Paolo Umari, and Renata M Wentzcovitch, “Quantum espresso: a modular and open-source software project for quantum simulations of materials,” *Journal of Physics: Condensed Matter* **21**, 395502 (2009).
- [44] P. Giannozzi, O Andreussi, T Brumme, O Bunau, M Buongiorno Nardelli, M Calandra, R Car, C Cavazzoni, D Ceresoli, M Cococcioni, N Colonna, I Carnimeo, A Dal Corso, S de Gironcoli, P Delugas, R A DiStasio, A Ferretti, A Floris, G Fratesi, G Fugallo, R Gebauer, U Gerstmann, F Giustino, T Gorni, J Jia, M Kawamura, H-Y Ko, A Kokalj, E Küçükbenli, M Lazzeri, M Marsili, N Marzari, F Mauri, N L Nguyen, H-V Nguyen, A Otero-de-la Roza, L Paulatto, S Ponce, D Rocca, R Sabatini, B Santra, M Schlipf, A P Seitsonen, A Smogunov, I Timrov, T Thonhauser, P Umari, N Vast, X Wu, and S Baroni, “Advanced capabilities for materials modelling with quantum espresso,” *Journal of Physics: Condensed Matter* **29**, 465901 (2017).
- [45] DR Hamann, “Optimized norm-conserving Vanderbilt pseudopotentials,” *Physical Review B* **88**, 085117 (2013).
- [46] Martin Schlipf and François Gygi, “Optimization algorithm for the generation of ONCV pseudopotentials,” *Computer Physics Communications* **196**, 36–44 (2015).
- [47] Cesar EP Villegas and Alexandre R Rocha, “Screened hydrogen model of excitons in semiconducting nanoribbons,” *Physical Review B* **109**, 165425 (2024).
- [48] Joshua JP Thompson, Samuel Brem, Marne Verjans, Robert Schmidt, Steffen Michaelis de Vasconcellos, Rudolf Bratschitsch, and Ermin Malic, “Anisotropic ex-



- citon diffusion in atomically-thin semiconductors,” *2D Materials* **9**, 025008 (2022).
- [49] David Vanderbilt, *Berry phases in electronic structure theory: electric polarization, orbital magnetization and topological insulators* (Cambridge University Press, 2018).
- [50] Adrien Bouhon, Tomáš Bzdusek, and Robert-Jan Slager, “Geometric approach to fragile topology beyond symmetry indicators,” *Phys. Rev. B* **102**, 115135 (2020).
- [51] M. Nakahara, *Geometry, Topology and Physics*, LLC (Taylor & Francis Group, 2003).
- [52] Junyeong Ahn, Sungjoon Park, Dongwook Kim, Youngkuk Kim, and Bohm-Jung Yang, “Stiefel-whitney classes and topological phases in band theory,” *Chinese Physics B* **28**, 117101 (2019).
- [53] Gianluca Panati, “Triviality of Bloch and Bloch–Dirac bundles,” *Annales Henri Poincaré* **8**, 995–1011 (2007).

## APPENDIX

### A. First principles calculations

We perform density functional theory calculations using the QUANTUM ESPRESSO package [43, 44] to study a family of polyacene chains. We use kinetic energy cutoffs of 80 Ry and 500 Ry for the wavefunction and charge density, respectively, and 12  $k$ -points to sample the Brillouin zone along the periodic direction. We use GGA (PBE) norm-conserving pseudopotentials which were generated using the code ONCVSP (Optimized Norm-Conserving Vanderbilt PseudoPotential) [45] and can be found online via the Schlipf-Gygi norm-conserving pseudopotential library [46]. We impose a vacuum spacing of 34.3 Å in the planar direction perpendicular to the polymer chain, and a vacuum spacing of 27.52 Å in the out-of-plane direction, to minimise interactions between periodic images of the polyacene chains. We perform a structural optimisation of the internal atomic coordinates to reduce the forces below 0.0015 Ry/Å.

We calculate the band structures of several polyacenes, as shown in Fig. 6. The hopping parameters of the SSH tight-binding model were deduced from these calculations. The SSH sites,  $A$  and  $B$ , on the molecular unit cell are illustrated with the red and blue boxes in Fig. 6(d), with the  $t_1$  hopping between them and the  $t_2$  hopping across the carbon link between unit cells [31]. While we do not employ GW calculations in our work, we note that the phase diagram in Fig. 2 would be quantitatively the same, and only the position of the individual molecules on the phase diagram could differ. In particular, it was found in previous works using GW [32] that the transition from trivial to topological electrons and holes could occur between the polypentacene ( $N = 5$ ) and polyheptacene ( $N = 7$ ) polymers, in contrast with our and previous [31] calculations, where the transition occurs between  $N = 3$  and  $N = 5$ .

### B. Wannier equation

We obtain the excitonic wavefunctions and associated bands by combining the electronic and hole states from the first principles DFT calculations with the envelope part of the excitonic wavefunction obtained by solving the Wannier equation.

We construct the electronic SSH Hamiltonian by Wannierising the electronic bands, from which  $t_1$  and  $t_2$  can be directly extracted. For each pair  $(t_1, t_2)$  we solve the Wannier equation:

$$\sum_{k'} h_{k,k'}(q) \psi_q^n(k) = E_n(q) \psi_q^n(k), \quad (11)$$

where  $\psi_q^n(k)$  is the envelope function of the  $n$ -th excitonic band. Moreover,

$$h_{k,k'}(q) = (E_{k+q/2}^e - E_{k-q/2}^h) \delta_{k,k'} - W_{k,-k',q}, \quad (12)$$

with electron/hole energies  $E^{e(h)} = E_{+(-)}$ , and the interaction matrix defined as:

$$W_{k,-k',q} = V_{\text{NR}}(k - k') \sum_{i,j \in \{A,B\}} \varphi_{i,k+q/2}^* \varphi_{j,k-q/2}^* \varphi_{j,k+q/2} \varphi_{i,k-q/2},$$

where  $\varphi_{i,k}$  is the wavefunction amplitude from the SSH model on site  $i$  with momentum  $k$ , and  $V_{\text{NR}}$  is the Coulomb potential for a one-dimensional system that describes the dielectric screening (see next Section for further details). We include the excitonic band dispersions for the lowest four excitonic bands  $E_n(q)$  of different polyacenes, as addressed in the main text, see Fig. 7.

### C. Dielectric screening model

The Wannier equation is highly dependent on the dielectric screening, where an accurate screening model is paramount to adequately capture the excitonic physics. In the polyacene chains, the Coulomb potential corresponds to that of one-dimensional nanoribbons, and following Ref. [47] and solving Poisson's equation, we arrive at the following form of the Coulomb potential:

$$V_{\text{NR}}(q) = \frac{e_0^2}{4\pi\epsilon_0} \frac{K_0(qL/2)}{\epsilon_s + 8q^2\alpha_{1D}K_0(qL/2)}, \quad (13)$$

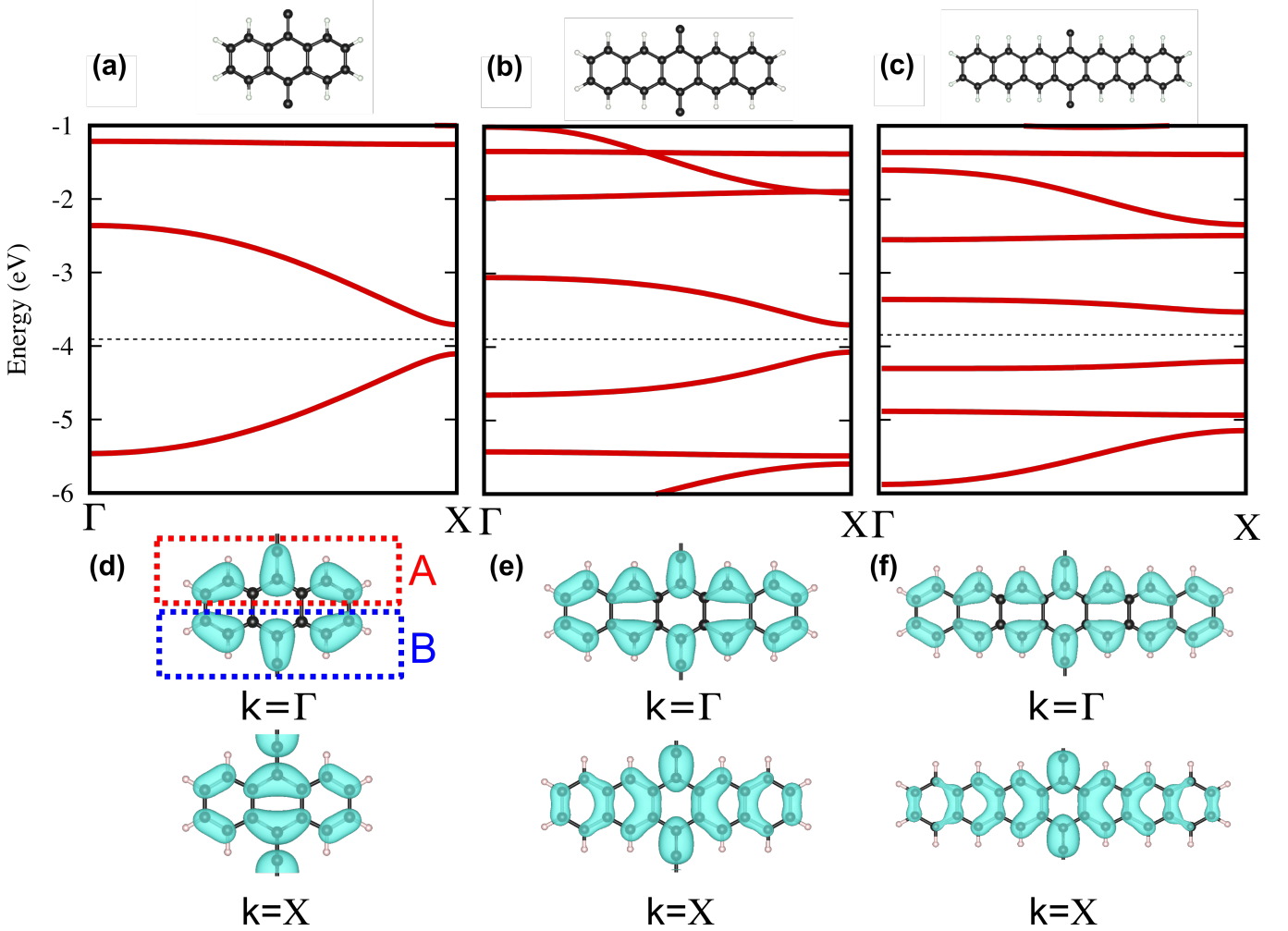


**FIG. 6.** Electronic bands in (a) polyanthracene, (b) polypentacene, and (c) polyheptacene, calculated using DFT. (d-f) Plots of the electronic wavefunctions for the valence band in the polyacenes. The shift of the charge centre, as well as the change of the parity of the wavefunction, as indicated by the inversion symmetry eigenvalues (on changing  $P_{\text{exc}} = 0$  to  $P_{\text{exc}} = 1$ ) can be directly observed in the DFT result. The approximate  $A$  and  $B$  sublattice sites in the molecular unit cells are marked with the red and blue boxes, respectively.

where  $L$  is the width of the ribbon,  $\alpha_{1D}$  is the screening parameter (polarisability per unit length),  $\epsilon_s$  is the background screening, and  $K_0$  is a modified Bessel function of the second kind. We take  $L$  to be the lateral size of the polyacene ribbon and fix  $\alpha_{1D} = 0.05 \text{ nm}^{-2}$  following previous work [47]. For small  $q$ , corresponding to long range interactions, the screening is dominated by the environment as determined by  $V_{\text{NR}}(q \rightarrow 0) \sim -\log(qL/2)/\epsilon_s$ . At large  $q$ , corresponding to short distances, the screening is approximately  $V_{\text{NR}}(q \rightarrow 0) \sim 1/(\alpha_{1D}q^2)$ , resembling the Coulomb interaction in bulk systems. The background screening  $\epsilon_s$ , defined as the average of the dielectric above and below the organic layer, further modulates the Coulomb interaction. We consider common background dielectrics in this work: vacuum ( $\epsilon_s = 1$ ),  $\text{SiO}_2$  substrate ( $\epsilon_s = 2.45$ ), and hBN encapsulation ( $\epsilon_s = 4.5$ ) [48].

#### D. Numerical excitonic Berry phases

To evaluate the excitonic Berry phases, we use a discretisation of the Brillouin zone  $q = [q(1), q(2), \dots, q(N_q)]$ , where we choose  $q(1) = 0$  and  $q(N_q) = 2\pi/a - \Delta q$ , with lattice parameter  $a$  and grid spacing  $\Delta q = 2\pi/(N_q a)$ . We use the parallel-transport gauge to numerically evaluate the Berry phase given by Eq. (2), following Ref. [49]:

$$\phi_{\text{exc}} = -\Im \log \left[ \left\langle u_{q(1)}^{\text{exc}} \left| u_{q(2)}^{\text{exc}} \right\rangle \dots \left\langle u_{q(N_q)}^{\text{exc}} \left| u_{q(1)}^{\text{exc}} \right\rangle \right]. \quad (14)$$

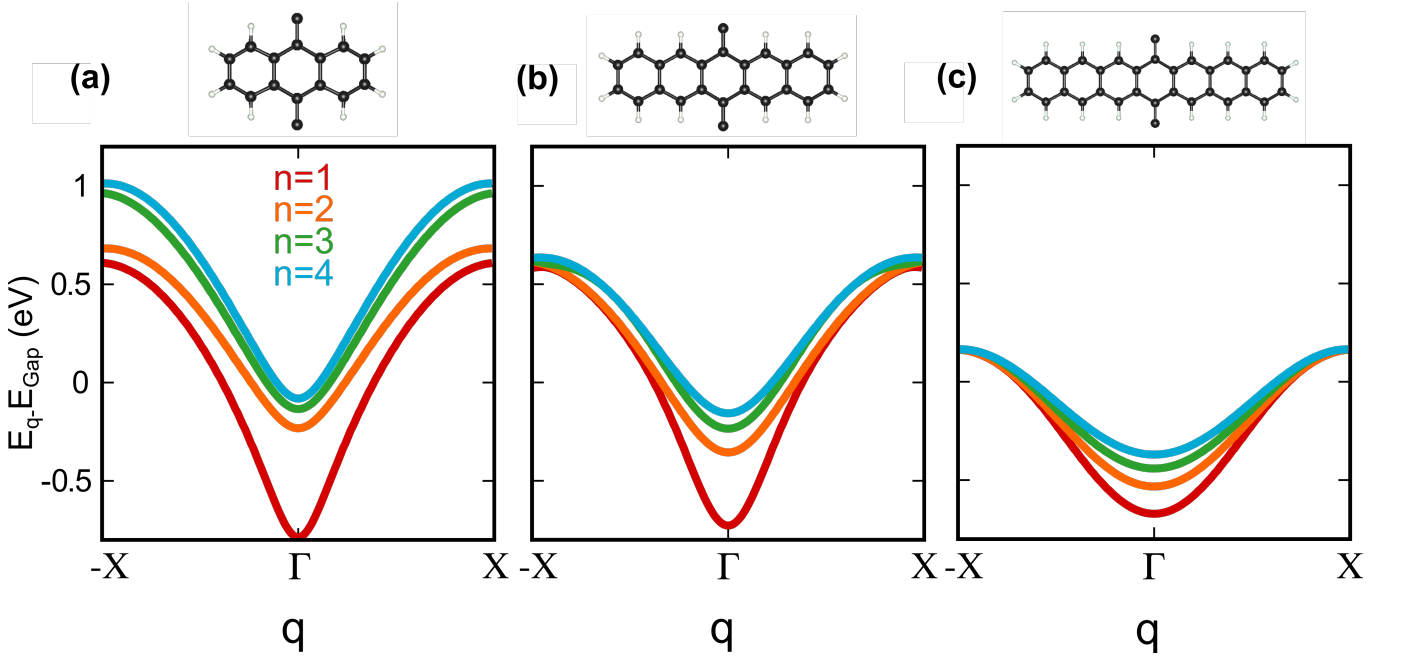


**FIG. 7.** Excitonic bands obtained from DFT single-particle states and the solution of the Wannier equation for the envelope function. We show the dispersion of the excitonic bands  $n = 1, 2, 3, 4$  of (a) polyanthracene ( $N = 3$ ), (b) polypentacene ( $N = 5$ ), and (c) polyheptacene ( $N = 7$ ). The excitonic bands are manifestly inversion-symmetric, while the excitonic bandwidths and dispersion decrease with increasing number of rings  $N$  in the monomers. We also note that as the excitonic bands approach the zero energy level, they merge into the continuum of electronic energies.

We use a  $q$ -grid of size  $N_q = 400$ , with convergence within a numerical error of  $\Delta\phi_{\text{exc}} \sim 10^{-3}$  for the excitonic Berry phase obtained above  $N_q = 200$ .

### E. Decomposition of the excitonic Berry connection

To compute the excitonic invariant  $P_{\text{exc}}$ , we utilise Eq. (1) and decompose the excitonic Berry connection of Eq. (2) into an envelope part and a single-particle part as:

$$A_{\text{exc}}(q) = A_{\text{exc}}^{\text{en}}(q) + A_{\text{exc}}^{\text{sp}}(q). \quad (15)$$

The envelope part reads:

$$A_{\text{exc}}^{\text{en}}(q) = i \sum_k \psi_q^*(k) \partial_q \psi_q(k), \quad (16)$$

and the single-particle part consists of the electron and hole contributions:

$$A_{\text{exc}}^{\text{sp}}(q) = \frac{1}{2} \sum_k |\psi_q(k)|^2 [A^e(k + q/2) + A^h(k - q/2)]. \quad (17)$$

In turn, the single-particle electron and hole Berry connections are given by  $A^{e/h}(k \pm q/2) = i \langle u_{k \pm q/2}^{e/h} | \partial_q u_{k \pm q/2}^{e/h} \rangle$ .

We find that in the hopping and interaction regimes realised by the organic materials in regions I and II, the contribution to  $\phi_{\text{exc}}$  due to the envelope part  $A_{\text{exc}}^{\text{en}}(q)$  vanishes, whereas the single-particle contribution  $A_{\text{exc}}^{\text{sp}}(q)$  due to the band geometry of the constituent electrons and holes (see ‘‘Riemmanian geometry of excitons’’ below), gives  $\phi_{\text{exc}} = \pi$  on integrating. However, in the limit of flat bands (region III), we find that  $A_{\text{exc}}^{\text{en}}(q)$  can provide an additional Berry phase contribution of  $\pi$ , trivialising the  $P_{\text{exc}}$  invariant. To explain such change explicitly, we thus detail an analytical argument for the previously numerically found trivialisation in the lowest exciton band, which we obtain by constructing a dualisation of an interacting SSH model in the flat-band limit [36] (see ‘‘Dualisation of the interacting Hamiltonian’’ below).

Moreover, beyond the numerical evaluation of the excitonic Berry phase and the dualisation argument detailed further below, we analytically model the topology of excitonic wavefunctions within the phase diagram by asserting an effective form of the excitonic envelope function. Explicitly, the exciton envelope function for the  $t_2 > t_1$  regime, obtained by a qualitative fit to the Wannier equation solution, reads:

$$\psi_q(k) = \mathcal{N} \left[ \cos(k+q)e^{-(k+q/2)^2/2} + \cos(k-q)e^{-(k-q/2)^2/2} \right], \quad (18)$$

with the normalisation constant  $\mathcal{N}$ . With this expression, we obtain a vanishing envelope contribution  $\oint dq A_{\text{exc}}^{\text{en}}(q) = 0$ , so that the excitonic topology is determined by the topology of the underlying electron and hole states.

For  $t_2 \gg t_1$ , we interestingly obtain  $\oint dq A_{\text{exc}}^{\text{en}}(q) = \pi$ , from an envelope function which was plotted in Fig. 8, a result we rationalise in the following theoretical modelling.

### F. Theoretical model

In this section we expand on the effective model discussed in the main text. We begin by building an electronic effective theoretical model based on the one-dimensional SSH Hamiltonian [29, 30]. We write Eq. (5) of the main text in the momentum-space Bloch orbital basis by introducing  $c_{Ak}^\dagger/c_{Bk}$ , on Fourier transforming the electronic creation and annihilation operators in the position basis  $c_{Ak}^\dagger = \frac{1}{\sqrt{L}} \sum_{j=1} e^{ik(r_e)_j} c_{A,j}^\dagger$ ,

$$H = \sum_{k;\alpha,\beta=A,B} [H^{\text{SSH}}(k)]_{\alpha\beta} c_{\alpha k}^\dagger c_{\beta k}. \quad (19)$$

with the electron position operator  $(r_e)_j = ja$ . In this basis, we have a Bloch Hamiltonian matrix which reads,

$$H^{\text{SSH}}(k) = \mathbf{d}(k) \cdot \boldsymbol{\sigma}, \quad (20)$$

where  $\mathbf{d}(k) = (t_1 + t_2 \sin k, t_2 \cos k, 0)^T$ , with  $\boldsymbol{\sigma} = (\sigma_x, \sigma_y, \sigma_z)$  the vector of Pauli matrices. The hopping parameters  $t_1$  and  $t_2$  can be retrieved to describe specific polyacenes by fitting them to the associated first principles calculations after Wannierisation. In this electronic model, the wavefunctions of electrons and holes take the compact form  $|u_k^{e/h}\rangle = \frac{1}{\sqrt{2|\mathbf{d}|^2}}(d_x \pm id_y, |d|)^T$ .

Having set up the electronic problem, we now elaborate on a theoretical model for the interaction-dependent excitonic topology. We start with a SSH-Hubbard-type model with up to the  $n^{\text{th}}$  neighbor interactions  $U_i$ , with  $i = 1, 2, 3, \dots, n$  in real space:

$$\begin{aligned} H = & \sum_j \epsilon_A n_{A,j} + \sum_j \epsilon_B n_{B,j} - t_1 \sum_j c_{A,j}^\dagger c_{B,j} + \text{h.c.} - t_2 \sum_j c_{A,j+1}^\dagger c_{B,j} + \text{h.c.} \\ & + \sum_j U_A n_{A,j} (n_{A,j} - 1) + \sum_j U_B n_{B,j} (n_{B,j} - 1) + \frac{1}{2} \sum_j \sum_{\alpha,\beta=A,B} \sum_{i=1}^n \left[ U_{2i-1}^{\alpha\beta} n_{\alpha,j-i} n_{\beta,j} + U_{2i}^{\alpha\beta} n_{\alpha,j+i} n_{\beta,j} \right], \end{aligned}$$

where the density operator reads,  $n_{A,j} = c_{A,j}^\dagger c_{A,j}$ , and within the tight-binding approximation for the Wannierised DFT-bands of the materials, we set the onsite energies to vanish,  $\epsilon_A = \epsilon_B = 0$ . Similarly, the onsite interaction terms of strength  $U_A, U_B$  vanish in a spin-polarised model, as no self-interactions should be included.

### G. Dualisation of the interacting Hamiltonian

To reflect the physics of the (screened) density-density interactions, we truncate the long-range interaction expansion at the level of the nearest-neighbor interactions  $U_1 \equiv U_1^{AB}$  and  $U_2 \equiv U_2^{AB}$  [36], assuming that  $U_1, U_2 \gg U_{i>2}$ . In the limit  $t_1, t_2 \gg U_1, U_2$ , we obtain the standard SSH model for electronic bands, and  $\oint dq A_{\text{exc}}^{\text{en}}(q) = 0$ . In this case, the entire contribution to excitonic topology can only emerge from the electrons and holes  $\oint dq A_{\text{exc}}^{\text{sp}}(q) = \pi$ . Intuitively, this corresponds to the formation of excitons on the same site where the constituent electrons and holes reside.

In the opposite limit,  $U_1, U_2 \gg t_1, t_2$ , the Hamiltonian reduces to:

$$H = \frac{U_1}{2} \sum_j [n_{A,j} n_{B,j} + n_{B,j} n_{A,j}] + \frac{U_2}{2} \sum_j [n_{A,j+1} n_{B,j} + n_{B,j} n_{A,j+1}] \quad (21)$$

Notably, we recognise that  $n_{B,j} = c_{B,j}^\dagger c_{B,j} = c_{B,j}^\dagger h_{B,j}^\dagger \equiv b_{B,j}^\dagger$ , where  $h_{B,j}^\dagger$  is a creation operator for a hole, and in combination with the creation operator of an electron  $c_{B,j}^\dagger$ , gives a localised exciton creation operator  $b_{B,j}^\dagger$ . Similarly, for sites  $A$  we write:  $n_{A,j} = c_{A,j}^\dagger c_{A,j} = h_{A,j} c_{A,j} \equiv b_{A,j}$ . On relabelling  $\frac{U_{1/2}}{2} \rightarrow -t_{1/2}^{\text{exc}}$ , we obtain a dualised SSH Hamiltonian for excitons:

$$H = -t_1^{\text{exc}} \sum_j b_{B,j}^\dagger b_{A,j} + \text{h.c.} - t_2^{\text{exc}} \sum_j b_{B+1,j}^\dagger b_{A,j} + \text{h.c.}, \quad (22)$$

where the Hubbard interactions between the electrons and holes on different sites effectively drive exciton hopping, or, in other words, exciton delocalisation. Notably, as  $t_{1/2}^{\text{exc}}$  are not independent from the electronic  $t_{1/2}$ , we observe no pocket where topological excitons would be obtained in the lowest excitonic band from trivial electrons and holes in [36] in the phase diagram, which would correspond to an additional region IV. The reason for the lack of such independence in the real material context (unlike in an abstract tight-binding model construction) is that both  $t_{1/2}$  and  $U_{1/2}$  are given by the matrix elements of the same Wannier states and local Hamiltonians, as well as (Coulomb) interaction potentials, and are therefore not independent. It should be noted here that the interactions manifestly do *not* break the inversion symmetry, by construction of the model.

Solving the excitonic Hamiltonian in region III for the eigenvectors  $|\psi_q^{\text{exc}}\rangle$  directly gives the SSH model eigenfunctions and associated Berry phases from the dualisation. As long as  $U_2 > U_1 \gg t_2 \gg t_1$ , the eigenvectors  $|\psi_q^{\text{exc}}\rangle$  host an excitonic Berry phase  $\phi_{\text{exc}} = \pi$  (or equivalently, for  $U_1 > U_2 \gg t_2 \gg t_1$ ,  $\phi_{\text{exc}} = 0$ ), independent from the electronic topology, as directly follows from the dualisation in the given flat-band limit. Hence, as the screening or  $t_2$  change, which abruptly changes  $U_1$  in the considered system, the  $\phi_{\text{exc}} = \pi$  due to  $t_2 \geq t_1$ , as contributed by  $A_{\text{exc}}^{\text{sp}}$  reduces to  $\phi_{\text{exc}} = 0$  with the increasing interaction. In particular, this crossover corresponds to the regime of the applicability of the limit for the retrieved dualisation, from which explicitly  $\phi_{\text{exc}} = 0$  follows.

## H. Topology in the strongly-polarised screening limit

Importantly, in the studied experimentally relevant organic systems,  $U_1, U_2$  can be controlled by screening, but  $U_2$  might be significantly lower than  $U_1$  ( $U_1 \gg U_2$ ) due to the chemistry of the material. Hence, in this setting only one part of the dualised-SSH phase diagram can be accessed. As a result, only a reduction to  $\phi_{\text{exc}} = 0$  can be achieved with the interactions in the present case. In case all parameters could be tuned freely, however, one could consider the case where  $U_2$  dominates  $U_1$ , which will achieve  $\phi_{\text{exc}} = \pi$ . This would yield topological excitons (in the lowest excitonic band) with trivial electrons and holes. This interesting scenario was recently pointed out in Ref. [36].

We now further consider the strongly-polarised limit when the screening is high, which drives an extension of the region III, with its boundary shifting such as when region II shrinks, see Fig. 2 of the main text. In particular, we provide further details on modelling and understanding the mismatch of electronic/hole, and excitonic Berry phases in that limit.

We begin by noting that in the limit of weak screened interactions, a photoexcitation introduces an electron-hole pair, by changing a population of two bands at given  $k$ -point, i.e.  $f_{nk} = 1 \rightarrow 0$  in the originally occupied band  $n$ , and  $f_{mk} = 0 \rightarrow 1$  at a given  $k$ -point in a zero-temperature limit. Any photoexcitation changes the polarisation in conduction and valence bands, as follows from the King-Smith-Vanderbilt formula within the modern theory of polarisation [37],

$$P_{c/v} = -e \int_{\text{BZ}} \frac{dk}{2\pi} f_{n/mk} i \langle u_{n/mk} | \partial_k u_{n/mk} \rangle = -\frac{e}{a} \bar{w}_{n/mk}, \quad (23)$$

which additionally relates the polarisation in the conduction ( $P_c$ ) or valence ( $P_v$ ) bands to the Wannier centres corresponding to these bands  $\bar{w}_{n,m}$ . In the context of electronic and hole Wannier centres, we have  $\bar{w}_e = \bar{w}_n$  and  $\bar{w}_h = \bar{w}_m$ . Here, the electron/hole Wannier centers are defined as [49]

$$\bar{w}_{e/h} = \langle w_0^{e/h} | r_{e/h} | w_0^{e/h} \rangle, \quad (24)$$

with the corresponding Wannier states obtained by Fourier-transforming electron and hole bands [49],

$$|w_0^{e/h}\rangle = \frac{a}{2\pi} \int_{\text{BZ}} dk e^{ikr_{e/h}} |u_k^{e/h}\rangle. \quad (25)$$

On the other hand, the excitonic Wannier center,

$$\bar{w}_{\text{exc}} = \langle w_0^{\text{exc}} | R | w_0^{\text{exc}} \rangle, \quad (26)$$

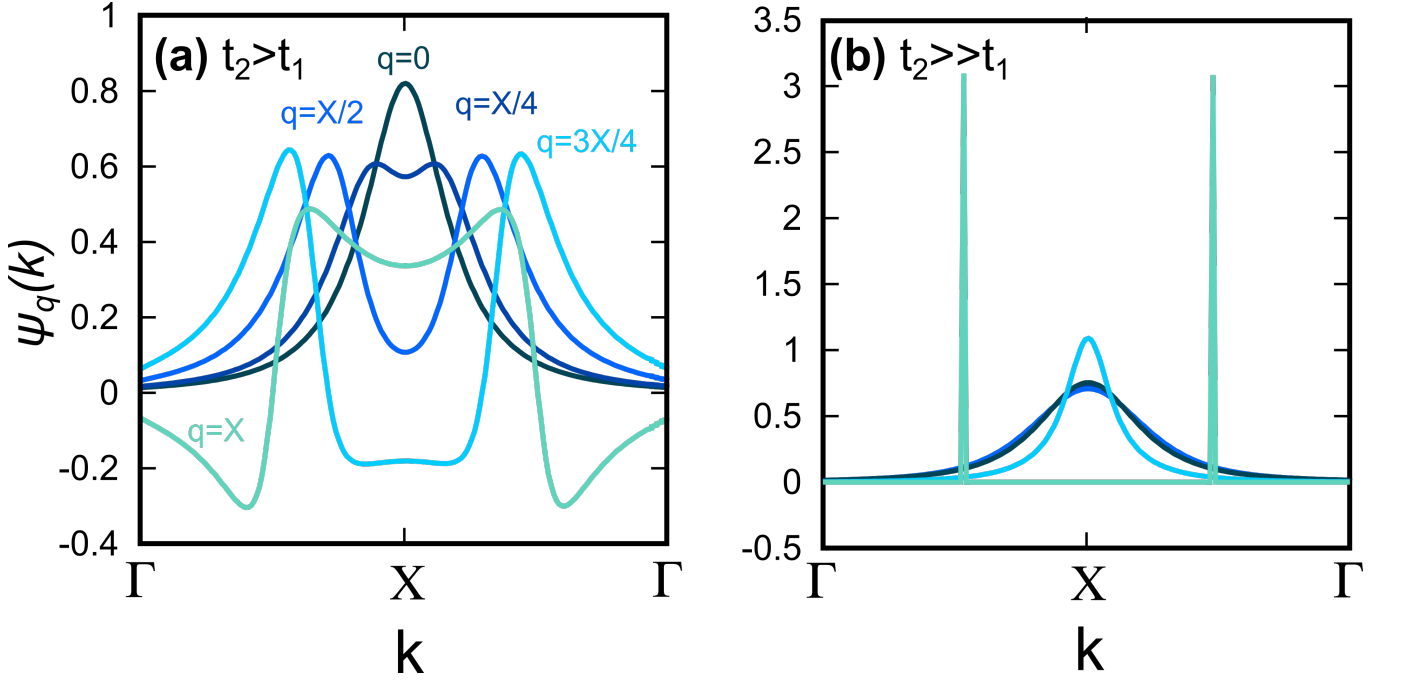


**FIG. 8.** (a) Excitonic envelope function for  $t_2 > t_1$ . There is no discontinuous change of  $\psi_q(k)$  as a function of  $q$ , yielding a vanishing contribution of  $A_{\text{exc}}^{\text{en}}$  to  $\phi_{\text{exc}}$ . In this regime, the topology of excitons is given purely by the topology of constituent electrons and holes, with electron and hole and exciton Wannier centres coinciding:  $\langle r_e \rangle = \langle r_h \rangle = \langle R \rangle$ . (b) Excitonic envelope function for  $U_2 \gg t_2 \gg t_1$ , the flat band limit. In this case,  $A_{\text{exc}}^{\text{en}}$  contributes  $\Delta\phi_{\text{exc}} = \pi$ , with electrons and holes shifted relative to the exciton centre, i.e.  $\langle r_e \rangle = 0$ ,  $\langle r_h \rangle = a$ ,  $\langle R \rangle = a/2$ , respectively. Here, two Dirac-delta-like functions develop out of a single peak, and correspondingly in real space we have  $\psi_q(r) \sim \cos(\frac{\pi}{a}r)$  on Fourier transforming, which shows that for a given  $q$ , the electron-hole separation  $r = r_e - r_h = a$  peaks at the length of the size of the unit cell, whereas, as a consequence, the probability density of finding the exciton center-of-mass is modulated periodically, and peaks at  $R = a/2 + ka$ , with  $k \in \mathbb{Z}$ , where the excitonic Wannier centres are present.

is defined with the excitonic Wannier states,

$$|w_0^{\text{exc}}\rangle = \frac{a}{2\pi} \int_{\text{BZ}} dq e^{iqR} |u_q^{\text{exc}}\rangle, \quad (27)$$

which are also pictorially represented in Fig. 3. Additionally, the relation between Berry phases and the Wannier centres gives  $\phi_{e/h} = 2\pi\bar{w}_{e/h}/a$ , which obtains the Berry phases for electron and holes. To obtain the Berry phase of the excitons  $\phi_{\text{exc}} = 2\pi\bar{w}_{\text{exc}}/a$  in the region III of the topological excitonic phase diagram, the Wannier equation is numerically solved. There, we numerically find  $\bar{w}_{e/h} = \frac{a}{2}$  for the fully occupied/unoccupied electron/hole band, alongside  $\bar{w}_{\text{exc}} = 0$  for the lowest excitonic polyacene (polypentacene, with the number of rings in the monomer  $N = 5$ , and polyheptacene, with  $N = 7$ ) bands, which can be understood as induced by pinning the electrons and holes across the unit cell with a strongly polar substrate (while respecting the inversion symmetry), such that the excitonic centre of mass  $R$  coincides with the origin of the unit cell  $\bar{w}_{\text{exc}} = 0$ .

### I. Riemannian geometry of excitons

In this section, we further elaborate on the Riemannian structure of the Bloch bundles of the excitonic wavefunctions and the associated excitonic quantum metric. We start by recognizing that we can equip a set, or bundle, of excitonic states  $|u_{\mathbf{q}}^{\text{exc}}\rangle$  with a Hermitian metric, known otherwise as a quantum-geometric tensor (QGT). Explicitly, we write [41]:

$$Q_{ij}^{\text{exc}} = \langle \partial_{q_i} u_{\mathbf{q}}^{\text{exc}} | 1 - \hat{P} | \partial_{q_j} u_{\mathbf{q}}^{\text{exc}} \rangle, \quad (28)$$

where  $\hat{P} = |u_{\mathbf{q}}^{\text{exc}}\rangle \langle u_{\mathbf{q}}^{\text{exc}}|$  is a projector onto the exciton band of interest. The excitonic QGT can be decomposed in terms of Riemannian (real) and symplectic (imaginary) parts. The imaginary part defines an excitonic Berry

curvature, which can be non-trivial only in two- or higher-dimensional systems, whereas the real part defines an excitonic Riemannian metric  $g_{ij}^{\text{exc}} \equiv \Re Q_{ij}^{\text{exc}}$ , which can be non-vanishing even in one-dimensional systems.

The metric defined as the real part of the QGT explicitly reads:

$$g_{ij}^{\text{exc}} = \frac{1}{2} \left[ \langle \partial_{q_i} u_{\mathbf{q}}^{\text{exc}} | \hat{Q} | \partial_{q_j} u_{\mathbf{q}}^{\text{exc}} \rangle + \langle \partial_{q_j} u_{\mathbf{q}}^{\text{exc}} | \hat{Q} | \partial_{q_i} u_{\mathbf{q}}^{\text{exc}} \rangle \right], \quad (29)$$

where  $\hat{Q} = 1 - \hat{P}$ . In the one-dimensional case, which we consider in this work, there exists a single excitonic metric component of interest:

$$\begin{aligned} g_{xx}^{\text{exc}} &= \frac{1}{2} \left[ \langle \partial_{q_x} u_{q_x}^{\text{exc}} | \partial_{q_x} u_{q_x}^{\text{exc}} \rangle - \langle \partial_{q_x} u_{q_x}^{\text{exc}} | u_{q_x}^{\text{exc}} \rangle \langle u_{q_x}^{\text{exc}} | \partial_{q_x} u_{q_x}^{\text{exc}} \rangle + \text{c.c.} \right] \\ &= \langle \partial_{q_x} u_{q_x}^{\text{exc}} | \partial_{q_x} u_{q_x}^{\text{exc}} \rangle - \langle \partial_{q_x} u_{q_x}^{\text{exc}} | u_{q_x}^{\text{exc}} \rangle \langle u_{q_x}^{\text{exc}} | \partial_{q_x} u_{q_x}^{\text{exc}} \rangle. \end{aligned} \quad (30)$$

We note that, on taking normalised eigenvectors  $\langle u_{\mathbf{q}}^{\text{exc}} | u_{\mathbf{q}}^{\text{exc}} \rangle = 1$ , and using the identity  $0 = \partial_q (\langle u_{\mathbf{q}}^{\text{exc}} | u_{\mathbf{q}}^{\text{exc}} \rangle) = \langle u_{\mathbf{q}}^{\text{exc}} | \partial_q u_{\mathbf{q}}^{\text{exc}} \rangle + \langle \partial_q u_{\mathbf{q}}^{\text{exc}} | u_{\mathbf{q}}^{\text{exc}} \rangle$ , we obtain  $\langle u_{\mathbf{q}}^{\text{exc}} | \partial_q u_{\mathbf{q}}^{\text{exc}} \rangle = -\langle \partial_q u_{\mathbf{q}}^{\text{exc}} | u_{\mathbf{q}}^{\text{exc}} \rangle$ . Hence, in the one-dimensional case of interest, and taking  $q \equiv q_x$ , i.e. dropping  $x$ -index for simplicity, we can also write,

$$g_{xx}^{\text{exc}} = \langle \partial_q u_q^{\text{exc}} | \partial_q u_q^{\text{exc}} \rangle - A_{\text{exc}} A_{\text{exc}}, \quad (31)$$

where  $A_{\text{exc}} = i \langle u_q^{\text{exc}} | \partial_q u_q^{\text{exc}} \rangle$ .

In general, the exciton quantum metric can be decomposed as:

$$g_{ij}^{\text{exc}}(\mathbf{q}) = g_{ij}^{\text{en}}(\mathbf{q}) + g_{ij}^{\text{sp-en}}(\mathbf{q}) + g_{ij}^{\text{sp}}(\mathbf{q}), \quad (32)$$

with the envelope contribution:

$$g_{ij}^{\text{en}}(\mathbf{q}) = \frac{1}{2} \sum_{\mathbf{k}} [\partial_{q_j} \psi_{\mathbf{q}}^*(\mathbf{k}) \partial_{q_i} \psi_{\mathbf{q}}(\mathbf{k}) + \partial_{q_i} \psi_{\mathbf{q}}^*(\mathbf{k}) \partial_{q_j} \psi_{\mathbf{q}}(\mathbf{k})] - A_{\text{exc}}^{\text{en},i} A_{\text{exc}}^{\text{en},j}, \quad (33)$$

the single-particle contribution:

$$g_{ij}^{\text{sp}}(\mathbf{q}) = \frac{1}{4} \sum_{\mathbf{k}} |\psi_{\mathbf{q}}(\mathbf{k})|^2 \left[ g_{ij}^{\text{e}}(\mathbf{k} + \mathbf{q}/2) + g_{ij}^{\text{h}}(\mathbf{k} - \mathbf{q}/2) \right] - A_{\text{exc}}^{\text{sp},i} A_{\text{exc}}^{\text{sp},j}, \quad (34)$$

and the mixed single-particle/envelope term:

$$g_{ij}^{\text{sp-en}}(\mathbf{q}) = \frac{1}{2} \sum_{\mathbf{k}} \left[ \partial_{q_i} |\psi_{\mathbf{q}}(\mathbf{k})|^2 \partial_{q_j} A_{\text{exc}}^{\text{sp},i} + \partial_{q_i} |\psi_{\mathbf{q}}(\mathbf{k})|^2 \partial_{q_j} A_{\text{exc}}^{\text{sp},j} \right] - \left[ A_{\text{exc}}^{\text{sp},i} A_{\text{exc}}^{\text{en},j} + A_{\text{exc}}^{\text{en},i} A_{\text{exc}}^{\text{sp},j} \right], \quad (35)$$

We note that the last term in each of the excitonic metric decomposition terms is the corresponding contribution from the excitonic Berry connection term, i.e. the second term from the decomposition of Eq. (31). In the above,  $g_{ij}^{\text{e/h}}(\mathbf{k})$  denote the individual single-particle quantum metrics of the electrons and holes. As mentioned in the main text, the envelope term  $g_{ij}^{\text{en}}$  becomes significantly enhanced in the higher excitonic bands, as it involves more pronounced variations of the corresponding excitonic envelope functions, see Fig. 5 for reference.

## J. Derivation of the bound on excitonic spread

The excitonic Riemannian metric encodes information about the localisation of the excitons, corresponding to the second moment, and in a one-dimensional context it is given by:

$$\xi^2 \equiv \text{Var}R = \langle R^2 \rangle - \langle R \rangle^2 = \frac{a}{2\pi} \int_{\text{BZ}} dq g_{xx}^{\text{exc}}(q), \quad (36)$$

where  $\langle (\dots) \rangle = \langle w_0^{\text{exc}} | (\dots) | w_0^{\text{exc}} \rangle$  and  $|w_j^{\text{exc}}\rangle = \frac{a}{2\pi} \int_{\text{BZ}} dq e^{-iqja} |\psi_q^{\text{exc}}\rangle$  is an excitonic Wannier state with lattice vector  $\mathbf{x} = ja$  labeling the unit cell of interest. Equation (36) follows by recognizing that Eq. (30) implies:

$$\begin{aligned} g_{xx}^{\text{exc}} &= \langle \partial_q u_q^{\text{exc}} | \partial_q u_q^{\text{exc}} \rangle - \langle \partial_q u_q^{\text{exc}} | u_q^{\text{exc}} \rangle \langle u_q^{\text{exc}} | \partial_q u_q^{\text{exc}} \rangle \\ &= \sum_m \langle \partial_q u_q^{\text{exc}} | u_{mq}^{\text{exc}} \rangle \langle u_{mq}^{\text{exc}} | \partial_q u_q^{\text{exc}} \rangle \\ &= \sum_m \langle \psi_q^{\text{exc}} | R | \psi_{mq}^{\text{exc}} \rangle \langle \psi_{mq}^{\text{exc}} | R | \psi_q^{\text{exc}} \rangle. \end{aligned}$$



This result follows by recognizing that for  $n \neq m$ , we have  $\langle \psi_{nq}^{\text{exc}} | R | \psi_{mq}^{\text{exc}} \rangle = i \langle u_{nq}^{\text{exc}} | \partial_q u_{mq}^{\text{exc}} \rangle$ , with  $|\psi_{mq}^{\text{exc}}\rangle = e^{iqR} |u_{mq}^{\text{exc}}\rangle$ , and where  $m$  runs over all excitonic band indices apart from the index of the band  $|u_q^{\text{exc}}\rangle$  of interest. Using the resolution of the identity  $1 = \sum_m |\psi_{mq}^{\text{exc}}\rangle \langle \psi_{mq}^{\text{exc}}| + |\psi_q^{\text{exc}}\rangle \langle \psi_q^{\text{exc}}|$ , we obtain,

$$g_{xx}^{\text{exc}} = \sum_m \langle \psi_q^{\text{exc}} | R | \psi_{mq}^{\text{exc}} \rangle \langle \psi_{mq}^{\text{exc}} | R | \psi_q^{\text{exc}} \rangle = \langle \psi_q^{\text{exc}} | R^2 | \psi_q^{\text{exc}} \rangle - \langle \psi_q^{\text{exc}} | R | \psi_q^{\text{exc}} \rangle \langle \psi_q^{\text{exc}} | R | \psi_q^{\text{exc}} \rangle. \quad (37)$$

Finally, on changing the basis according to  $|w_0^{\text{exc}}\rangle = \frac{a}{2\pi} \int_{\text{BZ}} dq e^{iqR} |u_q^{\text{exc}}\rangle$ , we obtain the following relationship between the excitonic quantum metric  $g_{xx}^{\text{exc}}$  and spread  $\xi^2$ :

$$\frac{a}{2\pi} \int_{\text{BZ}} dq g_{xx}^{\text{exc}} = \frac{a}{2\pi} \int_{\text{BZ}} dq \left( \langle \psi_q^{\text{exc}} | R^2 | \psi_q^{\text{exc}} \rangle - \langle \psi_q^{\text{exc}} | R | \psi_q^{\text{exc}} \rangle^2 \right) = \langle R^2 \rangle - \langle R \rangle^2 = \langle (R - \langle R \rangle)^2 \rangle = \text{Var} R \equiv \xi^2. \quad (38)$$

We now derive the main bound on the excitonic spread, captured by the excitonic metric due to the excitonic invariant  $P_{\text{exc}}$ . The excitonic  $\mathbb{Z}_2$  invariant under inversion ( $\mathcal{P}$ ) symmetry, in the gauge admitting only  $\phi_{\text{exc}} = 0/\pi$  under the symmetry, can be written as:

$$P_{\text{exc}} = \frac{1}{\pi} \int_0^{\pi/a} dq [A_{\text{exc}}(q) + A_{\text{exc}}(-q)] = \frac{1}{\pi} \int_0^{2\pi/a} dq A_{\text{exc}}(q). \quad (39)$$

We note, that in the studied organic materials, the excitonic states also satisfy the bosonic spinless time-reversal symmetry ( $\mathcal{T}^2 = 1$ ), culminating in the spinless spatiotemporal inversion symmetry,  $(\mathcal{PT})^2 = 1$  [50]. Therefore, topologically, the  $P_{\text{exc}}$  invariant corresponds to the first Stiefel-Whitney characteristic class  $w_1 \in \mathbb{Z}_2$  [50–52] of the (real) excitonic Bloch bundle. We now utilise the topological invariant associated with the mentioned characteristic class to demonstrate the quantum-geometric bound.

Correspondingly, we use a Cauchy-Schwarz inequality  $\left| \int dq f(q)g(q) \right|^2 \leq \left( \int dq |f(q)|^2 \right) \left( \int dq |g(q)|^2 \right)$ , with functions  $f(q) = 1$  and  $g(q) = A_{\text{exc}}(q)$ ,

$$P_{\text{exc}}^2 = \frac{1}{\pi^2} \left| \int_0^{2\pi/a} dq A_{\text{exc}}(q) \right|^2 \leq \frac{1}{\pi^2} \left( \int_0^{2\pi/a} dq' \right) \left( \int_0^{2\pi/a} dq |A_{\text{exc}}(q)A_{\text{exc}}(q)| \right) \leq \frac{2}{\pi a} \int_0^{2\pi/a} dq g_{xx}^{\text{exc}}(q), \quad (40)$$

where  $a$  is the lattice parameter. Here, we additionally recognise that in the maximally-smooth gauge extremising the overlaps of Bloch states between the neighbouring  $q$ -points,  $\langle u_q^{\text{exc}} | u_{q+\Delta q}^{\text{exc}} \rangle \approx 1 + \langle u_q^{\text{exc}} | \partial_q u_q^{\text{exc}} \rangle \Delta q \rightarrow 1$ , that obtains the maximally-localised Wannier functions [35]:  $|A_{\text{exc}}(q)A_{\text{exc}}(q)| = \langle \partial_q u_q^{\text{exc}} | \hat{P} | \partial_q u_q^{\text{exc}} \rangle \leq \langle \partial_q u_q^{\text{exc}} | \hat{Q} | \partial_q u_q^{\text{exc}} \rangle = g_{xx}^{\text{exc}}(q)$ , i.e. the overlap of  $|u_q^{\text{exc}}\rangle$  and  $|\partial_q u_q^{\text{exc}}\rangle$  is locally minimised, and is smaller than the overlap of  $|\partial_q u_q^{\text{exc}}\rangle$  with all the other exciton bands  $|u_{mq}^{\text{exc}}\rangle$  combined, as we also retrieve numerically. Intuitively, it should be noted that in the limit of a real gauge admitted under  $\mathcal{PT}$  symmetry, the former overlap approaches vanishingly small values locally, consistently with the metric evolving as  $g_{xx}^{\text{exc}}(q) = \langle \partial_q u_q^{\text{exc}} | \hat{Q} | \partial_q u_q^{\text{exc}} \rangle \rightarrow \langle \partial_q u_q^{\text{exc}} | \partial_q u_q^{\text{exc}} \rangle$ . Finally, on rearranging the derived inequality Eq. (40), we obtain,

$$\xi^2 \equiv \frac{a}{2\pi} \int_0^{2\pi/a} dq g_{xx}^{\text{exc}}(q) \geq \frac{a^2 P_{\text{exc}}^2}{4}, \quad (41)$$

showing that the maximally-localised excitonic Wannier functions support standard deviation associated with the spread:  $\xi \geq a/2$ , in the non-trivial phase with  $P_{\text{exc}} = 1$ . Mathematically, the non-trivial topological invariant  $P_{\text{exc}} = 1$  associated with the non-trivial first Stiefel-Whitney class  $w_1 \in \mathbb{Z}_2$  captures the orientability of a line subbundle of a real Bloch bundle [53], and is a global property of the excitonic Bloch bundles considered in this work. Intuitively, the non-trivial topology captured by the characteristic class implies the non-trivial quantum geometry locally, as a result of the associated non-orientability condition [51].